Contents list available at CBIORE journal website

International Journal of Renewable Energy Development

Journal homepage: https://ijred.cbiore.id

Research Article

Experimental analysis of a novel aerofoil-savonius type vertical axis wind turbine with an aerodynamic augmentation shell

Mohamad Hussein Farhat[1], Ahmad Sedaghat[2], Nader Ghareeb[2*], Mohamed El Badawy[2], Mohammad Nazififard[3,4], Ali Mostafaeipour[5]

[1] *Department of Electrical and Electronics Engineering, College of Engineering, Australian University, Safat 13015, Kuwait*

[2] *Department of Mechanical Engineering, College of Engineering, Australian University, Safat 13015, Kuwait*

[3] *Laboratoire Polytech'Lab (POLYTECH'LAB), Université Côte d'Azur, France*

[4] *Institut Polytechnique UniLaSalle, GeNumEr, UP 2018.C100, 14 Quai de la Somme, 80082 Amiens, France*

[5] *Civil and Environmental Engineering Department, California State University, Fullerton, California, USA*

Abstract. Savonius vertical axis wind turbines (SVAWTs) are attractive for urban and distributed energy applications because of their simple construction, omnidirectional wind acceptance, and self-starting capability, but their performance is limited by relatively low aerodynamic efficiency and high cut-in wind speeds. This study experimentally investigates a modified SVAWT that combines NACA0024 aerofoil sections at the blade extremities with an adjustable half-cylinder aerodynamic augmentation shell. The integrated configuration is evaluated as a proof-of-concept under controlled wind-tunnel conditions using both no-load and electrical-load measurements. The turbine was positioned at the exit of an open wind tunnel and tested over tunnel speeds of 9–18 m/s. The shell-assisted configuration reduced the cut-in tunnel speed from 12 to 9 m/s, increased rotational speed by up to 30%, and improved no-load voltage output by approximately 10–27%. Under resistive loading, the maximum power coefficient increased from 0.0086 to 0.0172 at 15 m/s, while peak electrical power increased by approximately 140% at 12 m/s, 100% at 15 m/s, and 68% at 18 m/s. The shell-assisted configuration also reduced the outlet-to-inlet velocity ratio and broadened the operating range over which higher torque coefficients were maintained. However, the tip-speed ratio remained below unity under all test conditions, and the absolute power coefficients were low because of the small prototype scale, low Reynolds number, absence of endplates, and rotor-generator constraints. The results demonstrate that the combined aerofoil-tip and shell configuration can provide measurable relative performance improvements compared with the same rotor operated without the shell. Further work is required to optimize the shell and aerofoil parameters, validate the flow mechanism directly, and assess performance at higher Reynolds numbers and under realistic urban wind conditions.

Keywords: Aerodynamic augmentation; Aerofoil-Savonius wind turbine; Power coefficient enhancement; Savonius rotor; Vertical axis wind turbine

Received: 19th June 2026; Revised: 19th August 2026; Accepted: 3rd Sept 2026; Available online: 10th Sept 2026

1. Introduction

The global transition towards sustainable energy has intensified the need for efficient small-scale renewable technologies suitable for urban and decentralised settings. Wind energy is one of the most mature renewable-energy technologies and is dominated by horizontal-axis wind turbines (HAWTs) for large-scale generation. However, deploying HAWTs in urban environments is constrained by mechanical complexity, noise, sensitivity to turbulent and multidirectional winds, and wildlife-safety concerns (Islam *et al.*, 2008; Simão Ferreira *et al.*, 2009).

Vertical-axis wind turbines (VAWTs) offer several advantages in such environments, including omnidirectional wind acceptance, mechanical simplicity, and reduced maintenance requirements (Brusca *et al.*, 2014). Among VAWTs, the Savonius rotor is particularly attractive because of its simple construction, robustness, low noise, and strong self-starting torque (Ushiyama & Nagai, 1988). Despite these advantages, Savonius turbines generally exhibit relatively low aerodynamic efficiency and higher cut-in wind speeds than lift-driven rotors (Altan & Atılgan, 2008; Kacprzak *et al.*, 2013). These limitations arise primarily from the adverse torque generated by the returning blade and from significant flow-separation losses.

To overcome these drawbacks, numerous performance-enhancement strategies have been investigated. For Savonius turbines, these include modifications to blade geometry, such as helical twist, Bach-type profiles, overlap-ratio optimisation, multi-stage configurations, and external flow-guiding structures (Roy & Saha, 2015; Mrigua *et al.*, 2020, 2022For lift-based VAWTs, performance enhancement has also been pursued through aerofoil-shape optimisation (Mohamed *et al.*, 2015). External augmentation devices, including ducts, deflectors, guide vanes, and shielding structures, can improve turbine

* Corresponding author
Email: n.ghareeb@au.edu.kw (N.Ghareeb)

performance by modifying the incident flow and reducing the adverse aerodynamic contribution of the returning blade (Kamoji *et al*., 2009; Mohamed *et al*., 2010; Ghareeb *et al*., 2026).

Significant progress has also been made in blade-profile optimisation for VAWTs. Mohamed (2012) investigated a range of aerofoil geometries and reported that the S-1046 profile improved the power coefficient by 26.83% relative to conventional NACA profiles in the investigated configuration. A combined CFD–DOE methodology applied to Savonius rotor geometry achieved a 22.8% increase in through guide-gap integration and parameter tuning (Al-Gburi *et al*., 2023). Other studies have examined adaptive blade shapes (Herath *et al*., 2015), the influence of pitch angle on VAWT performance (Rezaeiha *et al*., 2017), and CFD-based comparisons between Savonius and H-rotor Darrieus turbines (Ahmad & Rehman, 2023). These studies demonstrate that blade and aerofoil geometry can substantially influence torque generation, flow separation, and overall turbine performance (Shoukat *et al*., 2021).

In the present study, the NACA0024 profile was selected as a practical proof-of-concept aerofoil for integration at the Savonius blade extremities. Its symmetric geometry is suitable for a rotating blade section subjected to continuously changing relative-flow direction, while its relatively thick profile provides structural robustness and facilitates integration with the 3D-printed blade geometry. The 24% thickness also provides sufficient structural depth for additive manufacturing at the prototype scale. The present study does not claim that NACA0024 is aerodynamically superior to alternative profiles such as NACA0015, NACA0018, S-1046, or cambered aerofoils. Rather, it was selected as a suitable symmetric and manufacturable profile for evaluating the feasibility of the proposed integrated concept. Comparative optimisation of the aerofoil profile is therefore considered beyond the scope of the present study and is identified as an important direction for future investigation.

Research on external flow augmentation has likewise advanced considerably. Wong *et al.* (2017) reviewed the use of ducts, deflectors, and guide vanes for improving the performance of VAWTs and highlighted their potential to increase power density. Deda Altan and Gultekin (2023) reported that internal and external design modifications can provide substantial improvements in Savonius turbine performance. Aboujaoude *et al.* (2022) demonstrated significant increases in torque and power coefficients using an upstream deflector, while Kumar *et al.* (2024) reported performance gains using deflector plates as augmentation devices for a VAWT operating at wind speeds of 4–7 m/s. The importance of compact and efficient augmentation concepts for small wind turbines has also been emphasised in the broader review by Tummala *et al.* (2016).

Other approaches have focused on improving self-starting and low-speed operation. A combined Savonius–Darrieus turbine developed for irrigation applications demonstrated the benefit of incorporating a Savonius component to improve self-starting performance (Shahmari *et al*., 2020; Irawan *et al*., 2024). In the area of urban-compatible alternative designs, origami-inspired wind turbines have also been investigated, including configurations demonstrating low cut-in speeds (Farhat *et al*., 2025; Sedaghat *et al*., 2025). A subsequent experimental investigation of the same reaction-type concept reported a maximum power coefficient of at a tip-speed ratio of for a 10 cm diameter prototype (Sedaghat *et al*., 2026). Counter-rotating VAWTs have also been reviewed as a potential route towards improved efficiency, while highlighting the importance of environmental and siting considerations (Didane *et al*., 2024).

A critical examination of the existing literature indicates that Savonius turbine performance enhancement has generally followed two main approaches: rotor-level modifications, including blade-profile and geometric changes, and external augmentation devices, such as deflectors, guide vanes, ducts, and shielding structures. Although both approaches have demonstrated measurable performance benefits, their deliberate integration within a single experimentally evaluated Savonius-type system has received comparatively limited attention. In particular, few experimental studies have investigated the combination of aerofoil-shaped blade-tip sections with an adjustable external shell designed to modify the flow around the rotor and mitigate the adverse aerodynamic contribution of the returning blade.

The novelty of the present study therefore lies in the integration of these two augmentation strategies, rather than in either modification considered independently. The proposed configuration incorporates NACA0024 aerofoil sections at the blade extremities together with a movable half-cylinder aerodynamic shell positioned around part of the rotor. The shell is intended to alter the flow approaching the advancing and returning sides of the rotor, while the aerofoil-tip sections modify the aerodynamic behaviour of the blade extremities. Since direct flow-field measurements were not performed, the associated aerodynamic mechanisms are interpreted from the observed performance trends and established physical principles rather than treated as directly verified flow phenomena.

The scientific contribution of this work is the experimental evaluation of the integrated aerofoil-tip and adjustable-shell configuration under both no-load and electrical-load conditions. Performance is assessed using multiple complementary indicators, including cut-in wind speed, rotational speed, generated voltage, electrical power, power coefficient, and torque coefficient. The study is therefore presented as a proof-of-concept experimental investigation aimed at quantifying the relative performance changes produced by the combined configuration rather than establishing a fully optimized design. Systematic optimization of shell angle, rotor–shell gap, aerofoil chord ratio, and aerofoil position is reserved for future work. The results are also interpreted primarily as comparative laboratory-scale findings, since Reynolds-number scaling and performance under realistic urban wind conditions require further validation. The remainder of the paper is organised as follows. Section 2 describes the experimental methodology and apparatus, Section 3 presents the uncertainty-analysis framework, Section 4 presents and discusses the experimental results, and Section 5 summarises the principal conclusions.

2. Methodology

The experimental investigation was conducted using a custom-built test bench to evaluate the performance of a modified Savonius vertical axis wind turbine (SVAWT) incorporating NACA0024 aerofoil sections at the blade extremities and an adjustable aerodynamic augmentation shell. The rotor was manufactured by additive manufacturing, while the supporting structure was constructed from steel and aluminium components with telescopic extensions to permit adjustment of the turbine and shell positions. The rotor was directly coupled to a three-phase generator mounted beneath the turbine. The complete assembly was positioned externally at the exit of an open-circuit wind tunnel and tested over tunnel speeds ranging from 9 to 18 m/s.

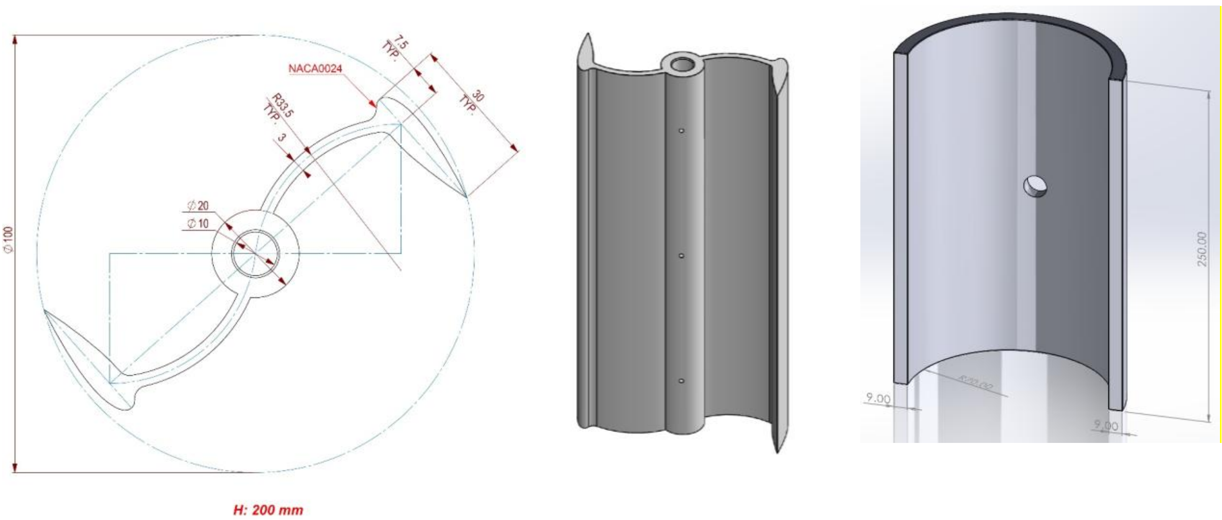

(a) (b) (c)

Fig. 1. SolidWorks design of the aerofoil-assisted SVAWT: (a) top-view engineering drawing (rotor Ø100 mm, blade radius R33.5 mm, NACA0024 aerofoil tip chord 30 mm, height H = 200 mm); (b) isometric view of the 3D-printed two-bladed rotor; (c) half-cylinder aerodynamic augmentation shell (height 250 mm, inner diameter 120 mm, edge gap 9 mm).

The laboratory temperature and relative humidity during the experiments were approximately 24 °C and 40%, respectively. An air density of 1.2 kg/m³ was adopted for the aerodynamic calculations. The principal measurements included inlet and outlet air velocity, rotor rotational speed, open-circuit voltage, and electrical power under controlled resistive loading. A handheld anemometer with an estimated uncertainty of ±0.5 m/s was used for airflow measurements, a digital tachometer with an uncertainty of ±10 RPM was used for rotational-speed measurements, and a multimeter with an uncertainty of ±0.1 V was used for voltage measurements. Electrical loading and power measurements were performed using an ET5407 programmable DC load with a power resolution of 1 mW. Before testing, the measuring instruments were checked for correct and consistent readings. Each experimental condition was measured in two independent runs. Because only two repetitions were available, the results are interpreted primarily as a controlled comparative dataset rather than as a basis for strong statistical inference.

2.1 Aerofoil-Assisted SVAWT Prototype

Fig. 1 presents the geometry of the two-bladed aerofoil-assisted SVAWT developed in SolidWorks and subsequently fabricated by 3D printing. The rotor has a diameter of 100 mm and a height of 200 mm, corresponding to an aspect ratio of 2.0. Each Savonius blade has a radius of 33.5 mm, while NACA0024 aerofoil sections with a chord length of 30 mm, equivalent to 30% of the rotor diameter, are incorporated at the blade extremities. The shaft hub diameters are 10 mm internally and 20 mm externally.

The NACA0024 profile was selected as a practical proof-of-concept geometry because of its symmetric section, relatively large thickness, structural robustness, and suitability for additive manufacturing. Its symmetric geometry is appropriate for a rotating blade section subjected to continuously changing relative-flow directions, while its 24% thickness facilitates structural integration with the Savonius blade at the prototype scale. The present study does not claim that NACA0024 represents the aerodynamically optimal aerofoil for this application; comparative evaluation of alternative symmetric and cambered profiles is reserved for future investigation.

The rotor was fabricated using a Flashforge Adventurer 3 Pro 2 printer with 1.75 mm PLA filament and a nozzle-temperature range of 190–220 °C. PLA was selected because of its dimensional stability, relatively low warping tendency, and suitability for reproducing the curved blade and aerofoil geometries.

2.2 Test Bench and Aerodynamic Shell

A custom test bench incorporating an adjustable aerodynamic shell was constructed, as shown in Fig. 2. Two steel plates measuring 600 × 600 mm and 2 mm in thickness were positioned at heights of 80 and 100 cm to support the generator and turbine assembly. A movable aluminium plate of similar dimensions was installed above the rotor, while the frame incorporated fixed and telescopic steel sections to enable positional adjustment. Four stainless-steel swivel caster wheels with manual brakes were used to facilitate positioning and secure the rig during testing.

The aerodynamic augmentation device consisted of a half-cylinder shell with an inner diameter of 120 mm and a height of 200 mm, matching the rotor height. With a rotor diameter of 100 mm, the shell provided a nominal radial clearance of approximately 10 mm between its inner surface and the rotor blade tips. The shell was mounted using a slotted support arrangement that permitted angular adjustment of approximately ±30° relative to the incoming flow direction.

Prior to the reported with-shell measurements, the shell angular position was adjusted experimentally while monitoring the rotor rotational speed. The position producing the highest observed RPM was selected and used for the subsequent measurements. This preliminary adjustment provided an experimental basis for selecting the shell orientation rather than assigning its position arbitrarily. However, the shell diameter, radial gap, arc length, and other geometric parameters were not

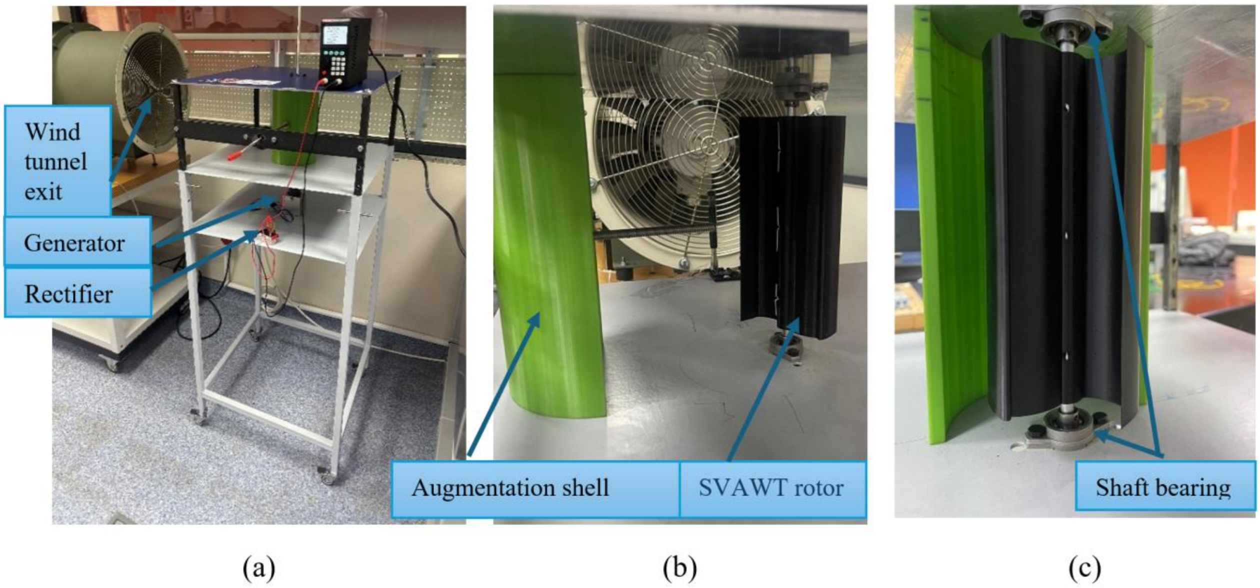

Fig. 2. Experimental test setup: (a) full test bench positioned at the GUNT HM 170 wind tunnel exit, showing the telescopic steel frame, ET5407 programmable DC load, and instrumentation; (b) side view of the black SVAWT rotor alongside the green aerodynamic augmentation shell, with the wind tunnel outlet visible in the background; (c) close-up of the two-bladed black rotor inside the green half-cylinder shell, showing the shaft flange bearings and shell-rotor radial gap.

subjected to a systematic parametric optimization. The configuration investigated in this study should therefore be considered a selected performance-oriented proof-of-concept configuration rather than a globally optimized shell design. A systematic study of shell angle, rotor–shell gap, shell dimensions, and aerofoil parameters is recommended for future work.

The selected shell orientation partially shielded the returning side of the rotor while leaving the advancing side exposed to the incoming airflow. The rotor was mounted on a 500 mm aluminium shaft with outer and inner diameters of 9 and 7 mm, respectively, and supported by two KFL000-type zinc-alloy miniature flange bearings with a 10 mm inner diameter.

2.3 Wind Tunnel and Flow Conditions

Experiments were performed using a GUNT HM 170 open-circuit wind tunnel equipped with a transparent test section measuring 420 × 292 × 292 mm and driven by a 3.4 kW motor. The tunnel provides nominal airflow velocities between approximately 1.3 and 25 m/s. Because the complete rotor-support arrangement could not be accommodated within the enclosed test section, the turbine test bench was positioned externally at the wind-tunnel outlet.

The external placement introduces experimental uncertainties associated with jet expansion, shear-layer development, spatial velocity non-uniformity, and increased turbulence relative to the enclosed test section. To characterize these conditions, airflow velocity was traversed across the outlet plane at the rotor hub height before turbine testing. The measured spatial variation across the region occupied by the rotor was less than approximately ±5%. Temporal variation in repeated anemometer readings indicated an estimated turbulence intensity of approximately 3–5%. These effects are therefore considered when interpreting the absolute turbine-performance coefficients.

The primary objective of the experiments was comparative evaluation. Both the with-shell and without-shell configurations were positioned at the same location relative to the wind-tunnel outlet and tested using identical tunnel-speed settings and measurement procedures. Consequently, although outlet-flow non-uniformity may influence the absolute measured values, its influence on the relative comparison between the two configurations is reduced.

Inlet velocity was measured with the anemometer positioned 50 mm upstream of the rotor leading edge at approximately mid-height. Three lateral measurement positions spanning the rotor diameter were used, and their average was taken as the representative inlet velocity. Outlet velocity was similarly measured 50 mm downstream of the rotor trailing edge at the same height and lateral positions. All reported inlet and outlet velocities therefore represent spatial averages of these three measurement points.

2.4 Blockage and Scaling Considerations

Because the turbine was positioned immediately downstream of the wind-tunnel outlet rather than inside a confined test section, conventional closed-test-section blockage corrections are not directly applicable. Nevertheless, a geometric area ratio can be estimated by comparing the projected rotor area with the nominal wind-tunnel outlet area.

The projected rotor area is

$$A_r = DH = 0.10 \times 0.20 = 0.020\, m^2 \tag{1}$$

while the nominal tunnel outlet area is

$$A_t = 0.292 \times 0.292 = 0.0853\, m^2 \tag{2}$$

The corresponding geometric area ratio is therefore

$$\beta = \frac{A_r}{A_t} \approx 0.235 \tag{3}$$

or approximately 23.5%.

This value should not be interpreted as a conventional closed-section blockage ratio because the rotor was located in an unconfined outlet jet, allowing lateral and vertical flow expansion. Furthermore, the aerodynamic shell modifies the local effective flow area and flow direction, making conventional blockage corrections inappropriate without detailed characterization of the external jet. The relatively high geometric area ratio is nevertheless acknowledged as a potential source of systematic uncertainty affecting the absolute Cp and CT values. Since both configurations were tested at the same position and under identical tunnel conditions, the with-shell versus without-shell comparison remains the principal basis for evaluating the augmentation effect.

The prototype represents a geometric scale of approximately 1:5 relative to a representative small urban turbine of 0.5 m diameter. With a rotor diameter of 100 mm, a rotor height of 200 mm, and measured inlet velocities of approximately 7–14 m/s, the blade-chord Reynolds number,

$$Re = \frac{\rho V c}{\mu} \quad (4)$$

ranges approximately from 1.4×10^4 to 2.8×10^4, using c = 30 mm, $\rho = 1.2$ kg/m³, and $\mu = 1.8 \times 10^{-5}$ kg/(m·s).

The experiments therefore fall within a low-Reynolds-number regime in which viscous effects, boundary-layer transition, and flow separation are more influential than in larger turbines operating at Re > 10^5 (Kamoji *et al.*, 2008). Consequently, the absolute aerodynamic coefficients measured in the present study should not be extrapolated directly to larger-scale turbines. The experimental results are used primarily to quantify the relative effect of adding the aerodynamic shell to the same aerofoil-assisted rotor under otherwise equivalent conditions.

2.5 Electrical Generator and Load

A three-phase brushless DC (BLDC) generator obtained from a small wind-turbine kit was directly coupled to the SVAWT rotor. The three-phase AC output was rectified to DC using a bridge rectifier consisting of six 1N5408 diodes rated at 3 A and 1000 V, followed by a 1000 μF, 50 V smoothing capacitor. Open-circuit and loaded voltages were measured using a multimeter.

Electrical loading was applied using an ET5407 programmable DC load operated in constant-resistance mode. Resistance was varied from approximately 30 to 2000 Ω to provide a range of electrical-loading conditions and identify the resistance corresponding to maximum electrical output at each investigated wind speed.

The generator internal resistance was measured as approximately 28 Ω. This relatively high internal resistance, together with mechanical losses in the shaft-bearing system and aerodynamic drag, imposes additional loading on the small rotor and is considered when interpreting the measured tip-speed ratios. Generator and rectifier losses were not independently separated from the overall electromechanical measurements and are therefore acknowledged as an additional uncertainty when relating measured electrical output to the aerodynamic performance of the rotor.

2.6 Geometric and Three-Dimensional Limitations of the Prototype

The experimental prototype is a single-stage rotor with an aspect ratio of 2.0 and without endplates. Consequently, the rotor is subject to three-dimensional blade-tip effects, including tip-vortex formation and associated induced losses. Such effects can reduce effective aerodynamic torque near the blade extremities and become proportionally more important for short-aspect-ratio rotors.

The absence of endplates may therefore contribute to the relatively low absolute values measured in the present experiments (Wang *et al.*, 2024). Larger-aspect-ratio turbines or configurations incorporating endplates may exhibit different aerodynamic characteristics. Accordingly, the present rotor should be regarded as a laboratory-scale proof-of-concept prototype rather than a dynamically scaled representation of a commercial SVAWT.

2.7 Experimental Procedure and Repeatability

Before each series of measurements, the measuring instruments were checked to confirm normal and consistent operation. The wind tunnel was then set to the required nominal speed. Following each change in wind speed, a stabilization period of approximately 30 s was allowed before measurements were recorded.

For the no-load experiments, the inlet and outlet velocities were measured using the three-point spatial procedure described in Section 2.3. Rotor rotational speed and open-circuit voltage were recorded after the respective readings had stabilized. For the electrical-load experiments, resistance was varied using the programmable DC load, and the corresponding stabilized rotational speed, voltage, and electrical power were recorded at each load condition.

The complete measurement procedure was performed for both with-shell and without-shell configurations under equivalent wind-tunnel conditions. Each experimental condition was independently repeated twice. The two repetitions were used to assess experimental repeatability and to calculate representative mean values and measurement dispersion.

The use of two repetitions constitutes a limitation of the present study because it provides limited statistical degrees of freedom for formal inferential analysis. Accordingly, the dataset is not used to make strong population-level statistical claims. Instead, repeatability, instrumental uncertainty, propagated uncertainty, and the magnitude and consistency of differences between the two configurations are considered jointly when interpreting the experimental results. A larger number of independent repetitions is recommended for future experimental validation.

3. Uncertainty Analysis and Theoretical Framework

Reliable interpretation of experimental turbine performance requires consideration of both measurement uncertainty and variability associated with the test environment and experimental arrangement. In the present study, uncertainty arises from instrumental resolution, repeated-measurement variability, wind-tunnel exit-flow non-uniformity, temporal aerodynamic fluctuations, probe positioning, rotor and shell alignment, generator and rectifier losses, and mechanical losses in the shaft-bearing system. The instrumentation used in the experiments and their estimated measurement uncertainties are summarized in Table 1. The uncertainty assessment follows the general principles of experimental uncertainty analysis (BIPM, 2023; Coleman *et al.*, 2010).

The uncertainty analysis was divided into two components: Type A uncertainty, derived from repeated measurements, and Type B uncertainty, associated with instrument resolution and known experimental-system effects. Because each operating condition was repeated twice, Type A estimates are used primarily as indicators of repeatability rather than as a basis for strong inferential statistical conclusions.

3.1 Type A Uncertainty from Repeated Measurements

For each pair of repeated measurements, the arithmetic mean was calculated as

$$\bar{x} = \frac{\Sigma x_i}{n} \quad (5)$$

where x_i is an individual measurement and n = 2 is the number of repetitions. The sample standard deviation was calculated as

$$s = \sqrt{[\Sigma(x_i - \bar{x})^2/(n - 1)]} \quad (6)$$

and the standard error of the mean was estimated as

$$SE = s/\sqrt{n} \quad (7)$$

Because only two repetitions were available, the resulting standard deviation and standard error have limited statistical degrees of freedom. They are therefore used to characterize experimental repeatability and to support comparative interpretation of the measurements, rather than to establish population-level statistical significance.

3.2 Type B and Experimental-System Uncertainty

In addition to instrumental uncertainty, several experimental-system effects may influence the measured turbine performance. The wind-tunnel outlet exhibited a spatial velocity variation of less than approximately ±5% across the rotor region, while temporal fluctuations corresponded to an estimated turbulence intensity of approximately 3–5%. These effects represent additional uncertainty associated with the external-jet arrangement.

Probe positioning introduces further uncertainty because inlet and outlet velocities were measured manually at three lateral locations. Small changes in probe location may therefore influence the spatially averaged velocity. Rotor and shell alignment may also introduce variability, particularly because shell position affects the local flow distribution around the rotor.

Additional uncertainty arises from the electromechanical system. Generator internal resistance, rectifier losses, bearing friction, and shaft alignment influence the relationship between aerodynamic rotor power and measured electrical output. Since these contributions were not independently quantified, they are treated as systematic experimental uncertainties and are considered when interpreting the absolute power coefficient (Cp) and torque coefficient (CT).

The principal additional uncertainty sources considered in the revised interpretation are wind-tunnel outlet non-uniformity, temporal flow fluctuations, anemometer positioning, rotor and shell alignment, shaft and bearing losses, generator internal resistance, rectifier losses, and repeatability between independent runs. These effects cannot all be reduced to a single numerical uncertainty using the available measurements. Accordingly, the reported error bars represent the quantified measurement and repeatability uncertainties, while the additional systematic effects are explicitly discussed as limitations affecting the absolute performance coefficients.

3.3 Uncertainty Propagation for Derived Quantities

For a derived quantity $y = f(x_1, x_2, \ldots, x_n)$, the combined uncertainty was estimated using the root-sum-square (RSS) method (Coleman *et al.*, 2010; Hughes & Hase, 2010):

$$u_Y = \sqrt{[(\partial y/\partial x_1 \cdot u_{x1})^2 + (\partial y/\partial x_2 \cdot u_{x2})^2 + \cdots + (\partial y/\partial x_n \cdot u_{xn})^2]} \quad (8)$$

where u_Y is the propagated uncertainty in the derived quantity y, and u_{xi} is the uncertainty associated with the measured variable x_i.

The percentage change between the shell-assisted and baseline configurations was calculated as

$$\Delta X(\%) = \frac{X_{shell} - X_{baseline}}{X_{baseline}} \times 100 \quad (9)$$

where Xshell and Xbaseline denote the corresponding measured quantities for the with-shell and without-shell configurations, respectively. The propagated uncertainty associated with this percentage change was estimated from the uncertainties of the two measured quantities using the RSS approach.

Similarly, the fractional velocity reduction across the rotor was calculated as

$$\eta_v = 1 - \frac{V_{out}}{V_{in}} \quad (10)$$

where Vin and Vout are the measured inlet and outlet air velocities, respectively. The uncertainty in ηv was propagated from the corresponding inlet- and outlet-velocity measurement uncertainties.

3.4 Statistical Interpretation

Because only two independent repetitions were available at each operating condition, formal inferential hypothesis testing was not considered statistically robust for the present dataset. In particular, paired t-tests or analysis of variance would have very limited statistical power with n = 2. The interpretation is therefore based on the magnitude and consistency of the measured differences, repeatability between runs, and propagated experimental uncertainty. This limitation is explicitly acknowledged, and future validation should employ a larger number of independent repetitions to permit statistically meaningful hypothesis testing and confidence-interval estimation. Accordingly, error bars in the revised figures are reported as ±1 standard deviation for repeated measurements or as propagated measurement uncertainty, as applicable. They are not interpreted as formal confidence intervals.

4. Results and Discussion

4.1 No-Load Results

4.1.1 Inlet and Outlet Velocity

Fig. 3 compares the mean inlet air velocity measured for the with-shell and without-shell configurations over wind-tunnel reference speeds ranging from 9 to 18 m/s. The inlet velocity increased approximately proportionally with wind-tunnel speed

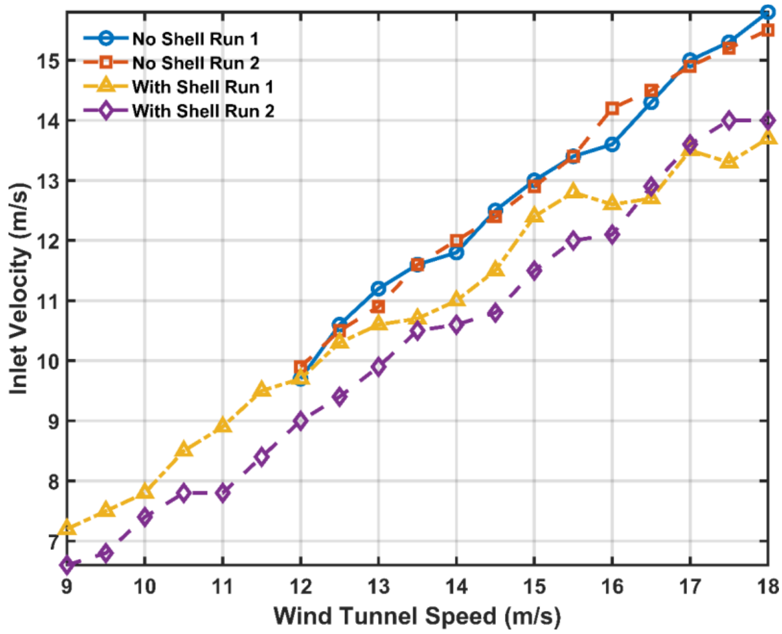

Fig. 3. Inlet air velocity as a function of wind-tunnel reference speed for the with-shell and without-shell configurations. Results from the two experimental runs are shown to indicate repeatability.

for both configurations. However, the measured inlet velocity was consistently lower when the aerodynamic shell was installed. At a wind-tunnel speed of 18 m/s, the mean inlet velocity decreased from approximately 15.5–15.8 m/s without the shell to approximately 13.7–14.0 m/s with the shell, corresponding to a reduction of about 12%.

The reduction in measured upstream velocity indicates that the shell alters the local flow field surrounding the rotor. Since direct pressure measurements, flow visualization, or CFD simulations were not performed, the detailed aerodynamic mechanism cannot be established from the present measurements alone. Nevertheless, the observed reduction is consistent with the shell producing a local obstruction and redistribution of the approaching flow. Such behaviour is also qualitatively consistent with previous Savonius augmentation studies in which external deflectors or shielding devices modified the flow reaching the advancing and returning blades (Mohamed *et al*., 2010; Aboujaoude *et al*., 2022).

Importantly, the shell-assisted turbine-initiated rotation at a wind-tunnel speed of 9 m/s, corresponding to a measured inlet velocity of approximately 7 m/s, whereas the configuration without the shell did not initiate sustained rotation until a wind-tunnel speed of approximately 12 m/s, corresponding to an inlet velocity of about 10 m/s. The reduction in cut-in condition therefore represents one of the clearest experimentally observed benefits of the shell-assisted configuration.

Fig. 4 compares the mean outlet velocities measured downstream of the rotor. Without the shell, outlet velocity

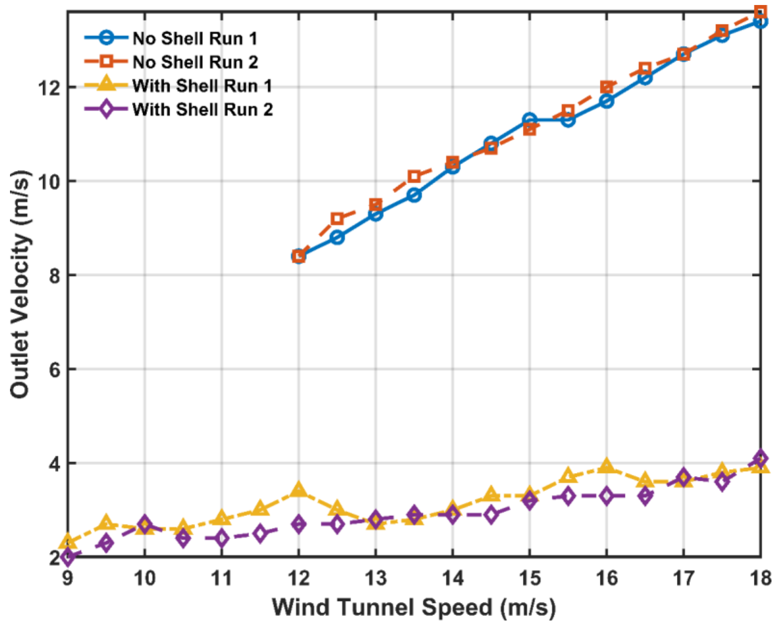

Fig. 4. Outlet air velocity as a function of wind-tunnel reference speed for the with-shell and without-shell configurations. Results from the two experimental runs are shown to indicate repeatability.

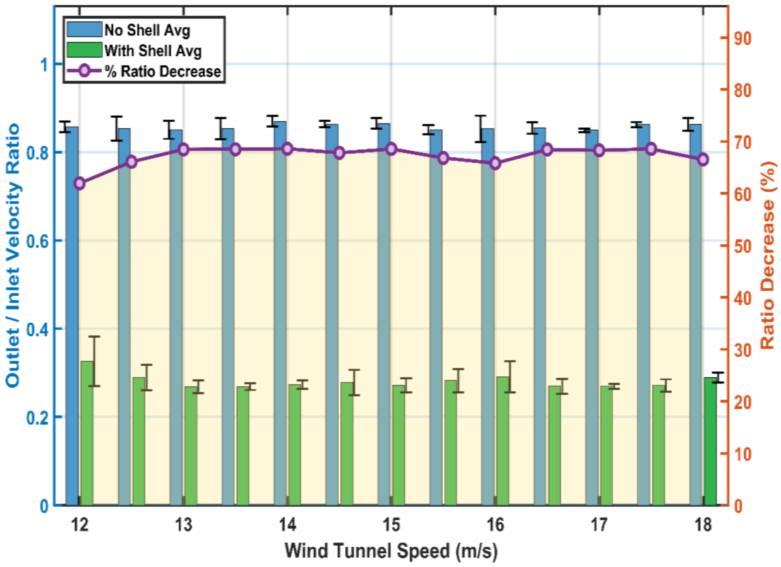

Fig. 5. Outlet-to-inlet velocity ratio versus wind tunnel speed for with- and without-shell configurations (left axis), and percentage reduction in ratio due to the shell (right axis). Error bars represent propagated measurement uncertainty (±1σ).

increased from approximately 8.4 m/s at a wind-tunnel speed of 12 m/s to approximately 13.4–13.6 m/s at 18 m/s. In comparison, the shell-assisted configuration exhibited substantially lower downstream velocities, increasing from approximately 2.0–2.3 m/s at 9 m/s to approximately 3.9–4.1 m/s at 18 m/s. At the highest investigated wind-tunnel speed, the measured outlet velocity was therefore approximately 70% lower for the with-shell configuration.

The large reduction in downstream velocity confirms that the presence of the shell substantially changes the velocity field downstream of the rotor. Although a lower downstream velocity is consistent with increased momentum extraction and/or flow diversion, it should not be interpreted directly as a quantitative measure of turbine energy extraction because the shell can redirect part of the flow laterally outside the measurement plane. The present outlet measurements are therefore used primarily as comparative indicators of the aerodynamic influence of the shell rather than as a direct measure of extracted mechanical power. This more cautious interpretation is important because the present experimental arrangement does not provide a complete velocity profile across the full downstream control surface. Direct flow-field measurements, such as PIV or CFD-supported control-volume analysis, would be required to separate actual rotor energy extraction from shell-induced flow redistribution.

To further compare the downstream-flow response, Fig. 5 presents the outlet-to-inlet velocity ratio, for both configurations over the common operating range of 12–18 m/s. For the turbine without the shell, the ratio remained approximately 0.85–0.86, indicating relatively little reduction in centreline-averaged velocity between the upstream and downstream measurement planes. In contrast, the shell-assisted configuration exhibited substantially lower ratios of approximately 0.29–0.33.

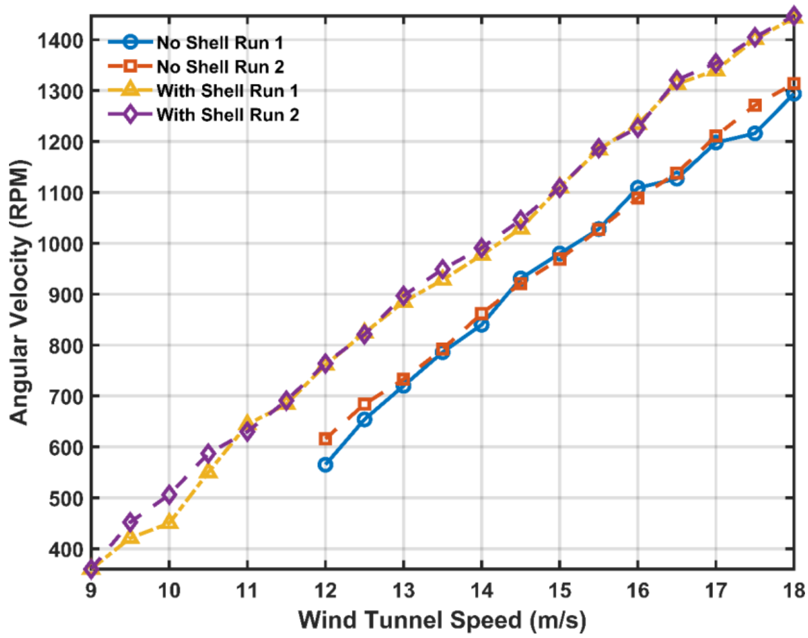

Fig. 6. Rotor angular velocity as a function of wind-tunnel reference speed for the with-shell and without-shell configurations. Results from the two experimental runs are shown to indicate repeatability

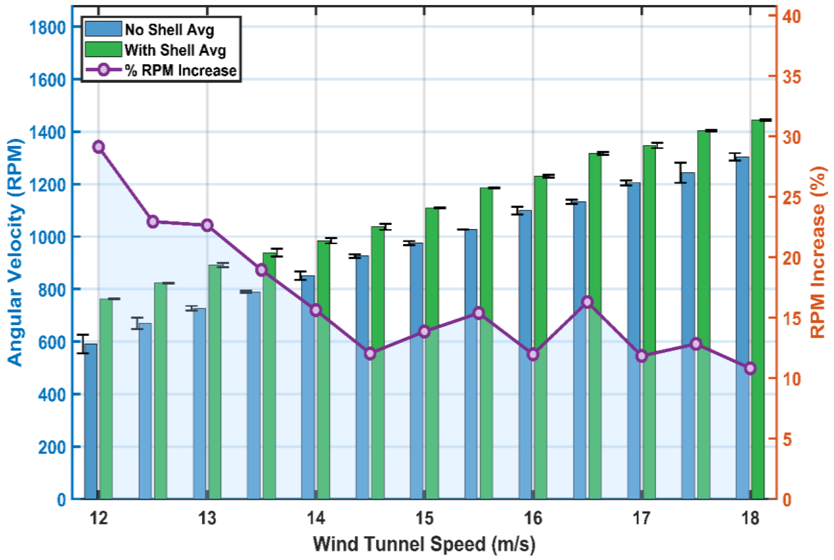

Fig. 7. Percentage increase in mean rotor angular velocity produced by the aerodynamic shell as a function of wind-tunnel reference speed. Error bars represent the propagated measurement and repeatability uncertainty. The largest relative improvement occurs near the baseline cut-in condition.

Relative to the baseline configuration, the outlet-to-inlet velocity ratio decreased by approximately 62–67% when the shell was installed. The relatively consistent reduction over the tested speed range indicates that the shell had a repeatable influence on the local flow field. However, because the shell can redirect airflow away from the downstream measurement locations, the ratio should be regarded as a local wake indicator rather than a direct measure of aerodynamic efficiency.

4.1.2 Angular Velocity

Fig. 6 presents the mean rotor angular velocity as a function of wind-tunnel reference speed for the with-shell and without-shell configurations. The shell-assisted turbine initiated sustained rotation at a wind-tunnel speed of 9 m/s, corresponding to an inlet velocity of approximately 7 m/s, whereas the turbine without the shell required approximately 12 m/s, corresponding to an inlet velocity of about 10 m/s. The shell therefore reduced the cut-in tunnel speed by approximately 3 m/s.

Above the cut-in condition, the shell-assisted turbine consistently achieved higher rotational speeds. At a wind-tunnel speed of 18 m/s, the with-shell configuration reached approximately 1443–1447 RPM, compared with approximately 1294–1314 RPM for the no-shell case. This represents a relative increase of about 10–12% at the highest investigated speed.

The largest relative increase occurred near the baseline cut-in condition. At 12 m/s, the shell-assisted turbine achieved an RPM increase of approximately 29–30% relative to the no-shell configuration. The relative benefit then decreased progressively as the wind-tunnel speed increased. This trend suggests that the shell provides its strongest assistance near the low-speed operating region, where the baseline rotor is only beginning to overcome aerodynamic and electromechanical resistance.

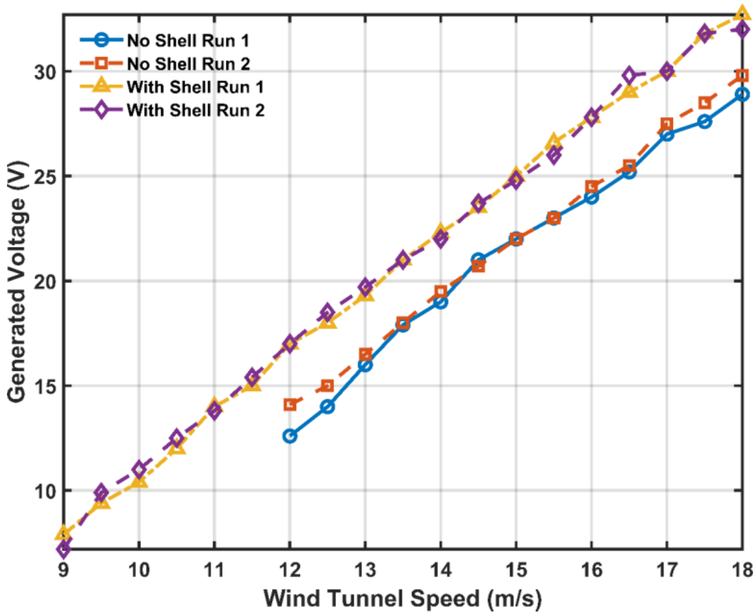

Fig. 8. Open-circuit voltage as a function of wind-tunnel reference speed for the with-shell and without-shell configurations. Results from the two experimental runs are shown to indicate repeatability.

The increase in RPM is consistent with the shell modifying the aerodynamic loading on the rotor and reducing the adverse influence of the returning side (Youssef *et al.*, 2020). However, because no direct flow-field or blade-pressure measurements were performed, the detailed mechanism responsible for the increase in rotational speed cannot be resolved from the present experiments alone. Fig. 7 presents the percentage increase in mean rotor angular velocity produced by the aerodynamic shell. The maximum improvement, approximately 29–30%, occurred at a wind-tunnel speed of 12 m/s. The relative increase decreased to approximately 11% at 18 m/s. The reduction in relative improvement with increasing wind speed indicates that the augmentation effect is most pronounced near the lower operating range. At higher wind speeds, the baseline rotor already reaches substantially higher rotational speeds, reducing the relative benefit provided by the shell. The observed trend may also reflect changes in aerodynamic loading, generator resistance, and mechanical losses as rotational speed increases. The two repeated runs showed close agreement, with run-to-run variation within approximately ±15 RPM. This supports the repeatability of the observed trend, although the limited number of repetitions prevents strong inferential statistical conclusions.

4.1.3 No-Load Voltage Output

Fig. 8 presents the mean open-circuit voltage as a function of wind-tunnel reference speed for the with-shell and without-shell configurations. The shell-assisted turbine began generating measurable voltage at a wind-tunnel speed of 9 m/s, corresponding to an inlet velocity of approximately 7 m/s, whereas the no-shell configuration required approximately 12 m/s, corresponding to an inlet velocity of about 10 m/s.

At 12 m/s, the shell-assisted configuration produced approximately 17 V compared with about 13.4 V for the no-shell case, corresponding to an increase of approximately 27.3%. At 13.5 m/s, the voltage increased from approximately 18 V without the shell to about 21 V with the shell, representing an improvement of approximately 17%. At 18 m/s, the measured voltage increased from approximately 29.4 V to 32.4 V, corresponding to an improvement of about 10.2%.

The voltage trend closely follows the rotational-speed results presented in Section 4.1.2. The larger voltage improvement observed near the lower operating range is consistent with the stronger relative increase in rotor speed produced by the shell near the baseline cut-in condition. As wind speed increases, the relative difference between the two configurations becomes smaller. Fig. 9 provides a direct comparison of the mean open-circuit voltage for the two configurations together with the corresponding percentage improvement due to the shell. The greatest relative increase occurs at 12 m/s, where the shell raises the generated voltage by approximately 27.3%. The percentage improvement then decreases progressively with increasing wind speed, reaching approximately 10.2% at 18 m/s. The repeated measurements showed consistent differences between the two configurations, and the observed voltage increases were larger than the nominal voltage-measurement uncertainty. This supports the conclusion that the shell-assisted configuration produced a repeatable improvement in generator output under no-load conditions.

4.2 Results Under Electrical Load

4.2.1 Power Output

Fig. 10 presents the electrical power output as a function of load resistance at wind-tunnel reference speeds of 12, 15, and 18 m/s for the with-shell and without-shell configurations. For all tested wind speeds, the electrical power initially increased with load resistance, reached a maximum, and subsequently decreased, indicating the presence of an operating resistance range associated with improved rotor generator matching.

At 12 m/s, the maximum electrical power increased from approximately 0.05 W without the shell to approximately 0.12 W with the shell, corresponding to an improvement of about 140%. At 15 m/s, the peak electrical power increased from approximately 0.16 W to 0.32 W, representing an improvement of about 100%. At 18 m/s, the maximum output increased from approximately 0.34 W to 0.57 W, corresponding to an improvement of approximately 68%. These results demonstrate that the shell-assisted configuration consistently produced higher electrical output over the investigated wind-speed range.

The relative benefit of the shell was greatest at the lowest loaded test speed and decreased as wind speed increased. This trend is consistent with the no-load rotational-speed and voltage results, which showed that the augmentation effect was strongest near the lower operating range. At higher wind speeds, the baseline turbine already operated at substantially

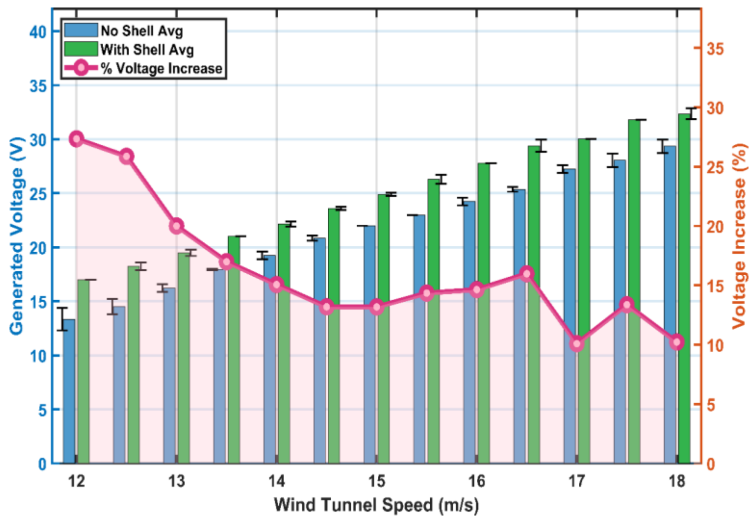

Fig. 9. Comparison of mean open-circuit voltage for the with-shell and without-shell configurations at each wind-tunnel reference speed. Percentage improvements due to the aerodynamic shell are indicated. Error bars represent the variability between repeated measurements.

ISSN: 2252-4940/© 2026. The Author(s). Published by CBIORE

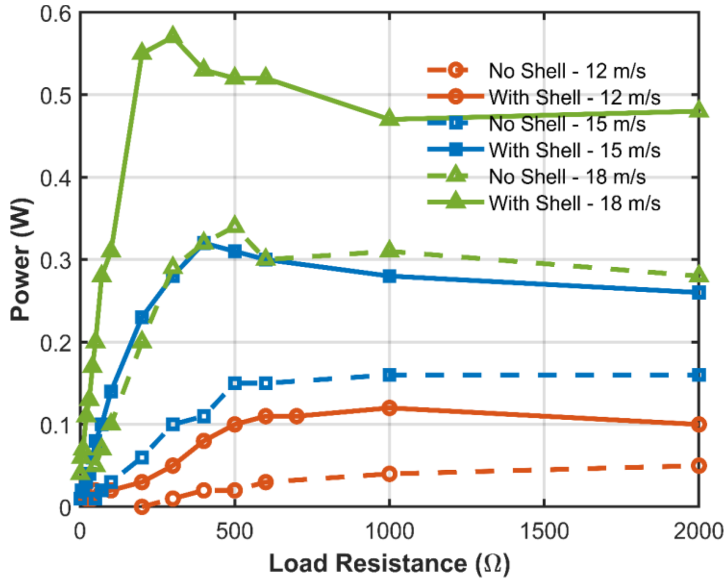

Fig. 10. Mean electrical power output as a function of load resistance at wind-tunnel reference speeds of 12, 15, and 18 m/s for the with-shell and without-shell configurations. Error bars represent the variability between repeated measurements. The shell-assisted configuration produces higher peak electrical power at all investigated wind speeds, with the largest relative improvement observed at 12 m/s.

greater rotational speed and electrical output, resulting in a smaller relative improvement.

The resistance corresponding to peak power also shifted toward lower values when the shell was installed. This behaviour indicates that the shell-assisted rotor was able to sustain increased electrical loading while maintaining higher rotational speeds. The effect is consistent with improved overall rotor–generator operating conditions, although the measured electrical output incorporates generator, rectifier, bearing, and other electromechanical losses that were not independently separated in the present study.

The reported power corresponds to the electrical output downstream of the generator and rectifier and therefore includes electromechanical conversion losses. However, the comparison between configurations remains valid because the same generator, rectifier, load, and experimental arrangement were used in both cases.

4.2.2 Power Coefficient

Fig. 11 presents the power coefficient, Cp, as a function of tip-speed ratio, λ, for the with-shell and without-shell configurations at wind-tunnel reference speeds of 12, 15, and 18 m/s. The shell-assisted configuration produced consistently higher Cp values over the investigated operating range. At 15 m/s, the maximum Cp increased from approximately 0.0086 without the shell to 0.0172 with the shell, corresponding to an improvement of about 100%. Similar relative improvements were observed at the other tested wind speeds.

The absolute Cp values obtained in the present experiments are substantially lower than the values commonly reported for larger or more aerodynamically optimized Savonius turbines. Several factors contribute to this result. First, the prototype operates in a low-Reynolds-number regime of

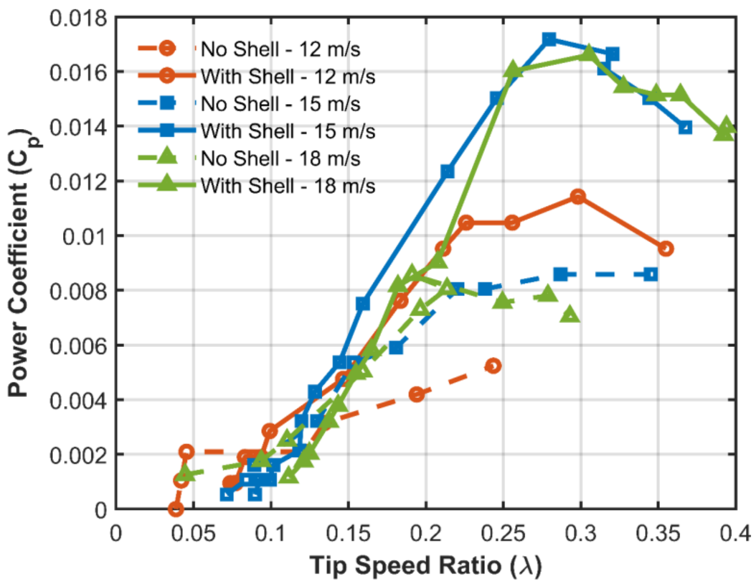

Fig. 11. Power coefficient, Cp, as a function of tip-speed ratio, λ, for the with-shell and without-shell configurations at wind-tunnel reference speeds of 12, 15, and 18 m/s. The shell-assisted configuration achieves higher Cp values and shifts the peak operating condition toward higher tip-speed ratios.

Table 2
Comparison of peak power coefficient, Cp, for the without-shell and with-shell configurations at each wind-tunnel reference speed.

Tunnel Speed (m/s)	Peak Cp @ R (No Shell)	Peak Cp @ R (With Shell)	Approximate Improvement (%)
12	0.0052 (R =2000 Ω)	0.0114 (R = 1000 Ω)	~119%
15	0.0086 (R = 1000 Ω)	0.0172 (R = 400 Ω)	~100%
18	0.0086 (R = 500 Ω)	0.0166 (R = 300 Ω)	~93%

approximately 1.4 × 10^4 to 2.8 × 10^4, where viscous effects and flow separation are more pronounced. Second, the rotor has a relatively low aspect ratio of 2.0 and was tested without endplates, increasing the influence of three-dimensional tip losses. Third, the turbine was directly coupled to a small generator with an internal resistance of approximately 28 Ω, introducing additional electromechanical loading. Finally, the reported Cp is derived from measured electrical output and therefore reflects generator, rectifier, bearing, and other conversion losses in addition to the aerodynamic performance of the rotor.

For these reasons, the absolute Cp values should be interpreted cautiously and should not be directly compared with values obtained from larger-scale turbines or from studies based on direct shaft-power measurements. The principal result of the present comparison is the relative improvement produced by the shell when the same rotor, generator, electrical system, and experimental arrangement are maintained.

The shell also shifted the operating point associated with peak Cp toward a higher tip-speed ratio. At 18 m/s, for example, the peak Cp occurred at approximately $\lambda = 0.19$ without the shell and approximately $\lambda = 0.30$ with the shell. This indicates that the shell-assisted rotor maintained improved performance at higher rotational speeds relative to the baseline configuration.

Although the aerodynamic shell increased the operating tip-speed ratio, λ remained below unity under all tested conditions. For example, at a wind-tunnel reference speed of 18 m/s, the shell-assisted rotor reached approximately 1445 RPM under no-load conditions. With a rotor radius of 0.05 m and a measured inlet velocity of approximately 14 m/s, this corresponds to $\lambda \approx 0.54$. Lower tip-speed ratios were obtained under electrical loading because the generator imposed additional braking torque on the rotor. The sub-unity TSR is therefore attributed to the combined influence of aerodynamic drag, low-Reynolds-number flow separation, mechanical losses in the shaft-bearing system, and electromechanical loading from the generator. The measured generator internal resistance of approximately 28 Ω provides further evidence of the electrical loading imposed on the small rotor.

Table 2 summarizes the peak Cp values and corresponding electrical-load resistance at each wind-tunnel reference speed. At 12 m/s, the peak Cp increased from 0.0052 without the shell to 0.0114 with the shell, corresponding to an improvement of approximately 119%. At 15 m/s, Cp increased from 0.0086 to 0.0172, corresponding to an improvement of approximately 100%. At 18 m/s, the peak Cp increased from 0.0086 to 0.0166, corresponding to an improvement of approximately 93%. Figs. 12(a) and 12(b) present heatmaps of Cp as a function of electrical-load resistance and wind-tunnel reference speed for the without-shell and with-shell configurations, respectively. The heatmaps provide a broader representation of the operating regions associated with higher power coefficients than the individual Cp–TSR curves alone. For the without-shell configuration, Cp remained below approximately 0.009 across the investigated range of wind speeds and load resistances. The highest values occurred at the intermediate and higher wind speeds, with the resistance associated with maximum Cp shifting toward lower values as wind speed increased.

The shell-assisted configuration exhibited consistently higher Cp values over a wider range of electrical loads. At wind-tunnel reference speeds of 15 and 18 m/s, Cp exceeded approximately 0.015 over a comparatively broad resistance range. This indicates that the improvement produced by the shell was not restricted to a single load condition but extended across several operating points. The shift toward lower optimal load resistance with the shell is also evident in the heatmaps and is consistent with the higher rotational speeds achieved by the augmented rotor. The broader high-Cp region indicates greater tolerance to changes in electrical loading and improved rotor–generator operating conditions over the investigated range.

4.2.3 Rotor Dynamics Under Load

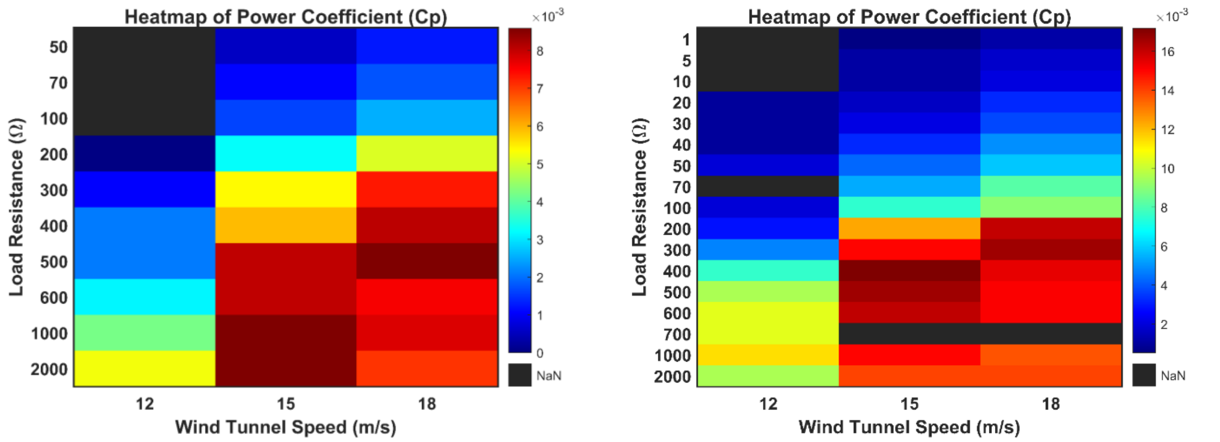

(a) (b)

Fig. 12. Heatmaps of power coefficient, Cp, as a function of electrical-load resistance and wind-tunnel reference speed for (a) the without-shell configuration and (b) the with-shell configuration. The shell-assisted configuration produces a broader operating region with elevated Cp values.

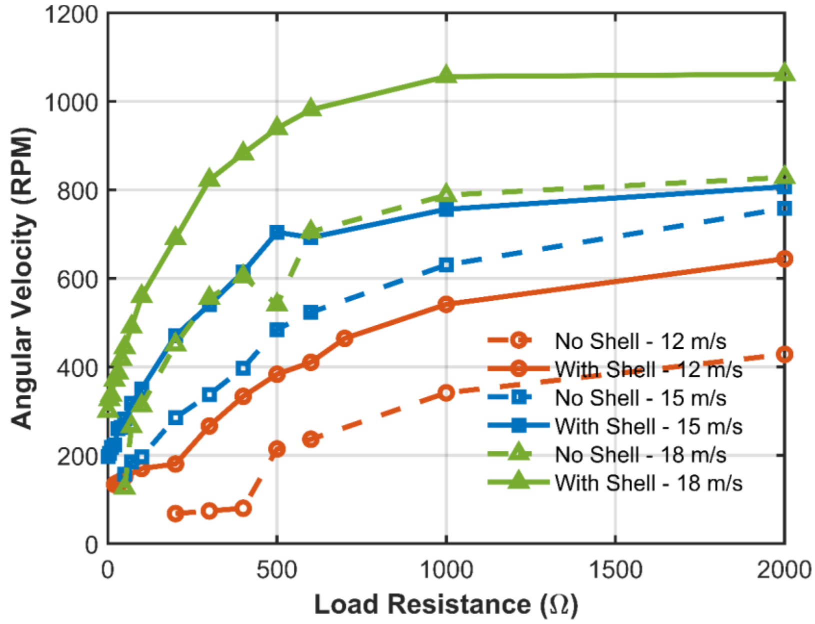

Fig. 13. Rotor angular velocity as a function of electrical-load resistance at wind-tunnel reference speeds of 12, 15, and 18 m/s for the with-shell and without-shell configurations.

Fig. 13 presents the rotor angular velocity as a function of electrical-load resistance at wind-tunnel reference speeds of 12, 15, and 18 m/s for the with-shell and without-shell configurations. At all tested wind speeds, rotor speed increased as the electrical resistance increased, reflecting the reduction in generator loading at higher resistance values.

At 12 m/s, the shell-assisted turbine operated over approximately 134–644 RPM across the investigated resistance range, compared with approximately 68–428 RPM for the without-shell configuration. The relative improvement was particularly pronounced at low resistance values, where the shell-assisted rotor maintained substantially higher rotational speed under heavier electrical loading.

At 15 m/s, the same trend was observed. For example, at a load resistance of 500 Ω, the rotor speed increased from approximately 484 RPM without the shell to about 704 RPM with the shell, corresponding to an improvement of approximately 45%. At 18 m/s, the shell-assisted configuration maintained approximately 40–50% higher rotational speed over a broad resistance range of roughly 300–1000 Ω.

These results show that the shell-assisted configuration improves the ability of the rotor to maintain rotational speed under electrical loading. The effect is particularly important at lower resistance values, where the generator exerts stronger braking torque on the rotor. The higher rotational speed maintained by the with-shell configuration under these

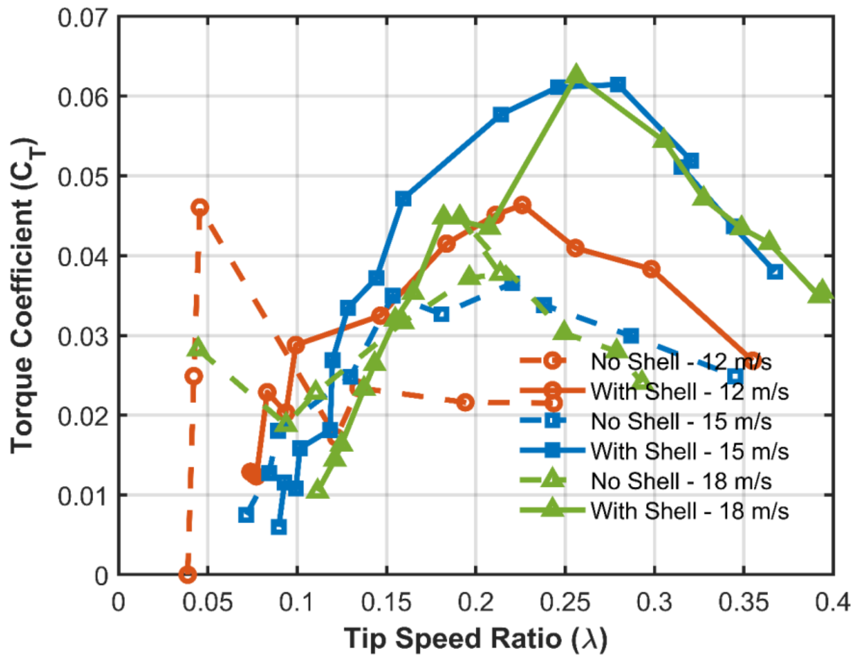

Fig. 14. Torque coefficient (CT) versus tip speed ratio (λ) for with- and without-shell configurations at tunnel speeds of 12, 15, and 18 m/s. The shell improves peak CT and sustains high torque over a wider TSR range.

Table 3
Comparison of peak torque coefficient, CT, for the without-shell and with-shell configurations at each wind-tunnel reference speed.

Tunnel Speed (m/s)	Peak CT @ R (No Shell)	Peak CT @ R (With Shell)	Approximate Improvement (%)
12	0.0461 (R = 400 Ω)	0.0463 (R = 600 Ω)	~0% (shell broader peak)
15	0.0365 (R = 500 Ω)	0.0614 (R = 400 Ω)	~68%
18	0.0448 (R = 500 Ω)	0.0625 (R = 200 Ω)	~40%

conditions is consistent with the higher electrical power output reported in Section 4.2.1.

4.2.4 Torque Coefficient

Fig. 14 presents the torque coefficient, CT, as a function of tip-speed ratio, λ, for the with-shell and without-shell configurations at wind-tunnel reference speeds of 12, 15, and 18 m/s. The shell-assisted configuration generally produced higher CT values and maintained elevated torque over a wider range of tip-speed ratios.

At 12 m/s, the without-shell turbine reached a peak CT of approximately 0.046 at a relatively low tip-speed ratio, after which CT decreased as rotational speed increased. The shell-assisted configuration achieved a similar peak magnitude, approximately 0.046, but maintained higher torque over a broader operating range. This indicates that, although the peak torque coefficient was not substantially increased at 12 m/s, the shell improved the range over which useful torque could be sustained.

At 15 m/s, the benefit became more pronounced. The shell-assisted turbine reached a peak CT of approximately 0.061 at a load resistance of 400 Ω, compared with approximately 0.037 for the without-shell configuration at 500 Ω. This corresponds to an improvement of about 68%. The shell-assisted rotor also maintained CT above approximately 0.05 over a wider resistance range. At 18 m/s, the peak CT increased from approximately 0.045 without the shell to approximately 0.063 with the shell, corresponding to an improvement of about 40%. The with-shell configuration also maintained elevated CT values over a broader range of tip-speed ratios and electrical loads.

The broader high-CT operating region is important because it indicates that the shell-assisted rotor is less sensitive to changes in electrical loading. In particular, the shell configuration maintained measurable torque even at relatively low resistance values, where the generator imposed stronger electrical braking. This behaviour is consistent with the higher rotational speeds observed under load in Section 4.2.3.

Table 3 summarizes the maximum CT values obtained at each wind-tunnel reference speed. At 12 m/s, the peak CT values were nearly identical, with 0.0461 for the without-shell configuration and 0.0463 for the with-shell configuration. However, the shell-assisted turbine maintained high CT over a broader resistance range. At 15 m/s, peak CT increased from 0.0365 to 0.0614, corresponding to an improvement of approximately 68%. At 18 m/s, peak CT increased from 0.0448 to 0.0625, corresponding to an improvement of approximately 40% Figs. 15(a) and 15(b) present heatmaps of CT as a function of load resistance and wind-tunnel reference speed for the without-shell and with-shell configurations, respectively. The without-shell turbine exhibited relatively narrow regions of elevated CT, while the shell-assisted configuration showed a broader high-CT operating region, particularly at 15 and 18 m/s. At 15 m/s, the shell-assisted turbine-maintained CT above approximately 0.05 over a resistance range of about 100–600 Ω. At 18 m/s, CT remained above approximately 0.04 over a broad range of approximately 30–600 Ω. The heatmaps therefore confirm that the shell improves not only the peak torque coefficient at the higher tested wind speeds but also the range of electrical-loading conditions over which elevated torque is maintained.

4.3 Comparison with Previous Savonius Augmentation Studies

The performance improvement observed in the present study is consistent with the general trend reported for Savonius

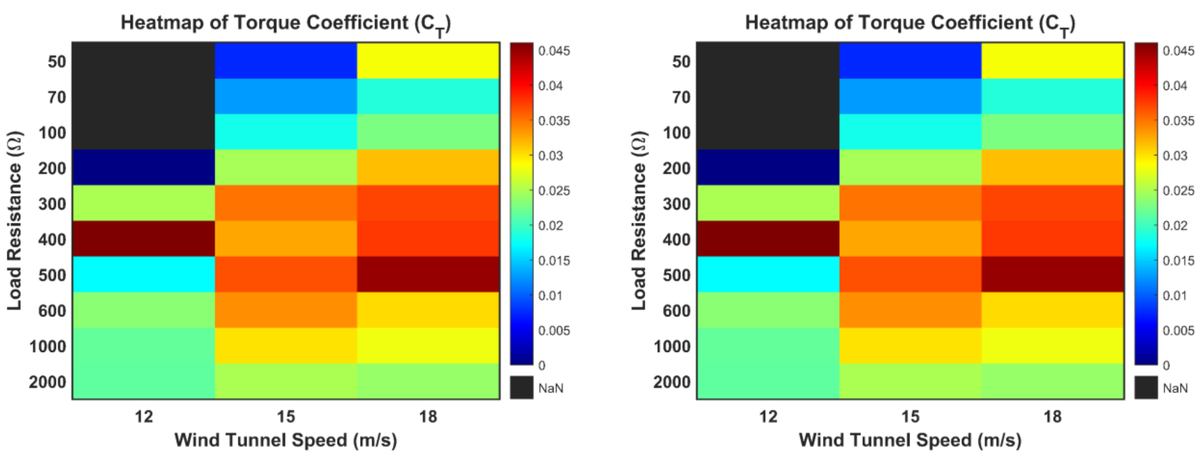

(a) (b)

Fig. 15. Heatmaps of torque coefficient, CT, as a function of electrical-load resistance and wind-tunnel reference speed for (a) the without-shell configuration and (b) the with-shell configuration. The shell-assisted configuration broadens the operating region associated with elevated CT values.

Table 4.
Comparison of the present study with representative Savonius turbine performance-enhancement studies.

Study	Enhancement approach	Reported performance improvement
Mohamed (2012)	Aerofoil-profile optimization	26.83% improvement in Cp
Al-Gburi *et al.* (2023)	Rotor-geometry and guide-gap optimization	22.8% improvement in Cp
Deda Altan and Gultekin (2023)	Internal and external augmentation concepts	Significant improvement in Savonius performance
Aboujaoude *et al.* (2022)	Upstream aerodynamic deflector	Improvement in torque and power coefficients
Present study	NACA0024 blade-tip sections with adjustable half-cylinder shell	93–119% increase in peak Cp

turbine modification and external-flow augmentation, although direct comparison of absolute Cp values requires caution because of differences in rotor geometry, Reynolds number, experimental arrangement, and power-measurement methodology. Mohamed (2012), for example, reported a 26.83% improvement in power coefficient through aerofoil-profile optimization, while Al-Gburi *et al.* (2023) achieved a 22.8% increase in Cp through combined rotor-geometry and guide-gap optimization. External augmentation approaches have also demonstrated substantial performance benefits. Deda Altan and Gultekin (2023) reported that the addition of external guide structures can significantly increase Savonius turbine performance, while Aboujaoude *et al.* (2022) demonstrated improved torque and power coefficients using an upstream deflector.

In the present study, the aerodynamic shell increased the peak Cp by approximately 119% at 12 m/s, 100% at 15 m/s, and 93% at 18 m/s relative to the same aerofoil-assisted rotor operating without the shell. These relative improvements are substantial; however, the absolute Cp values remain lower than those reported for many conventional or optimized Savonius turbines. The difference is associated with the low Reynolds number of the present prototype, its aspect ratio of 2.0, the absence of endplates, the external wind-tunnel arrangement, and the inclusion of generator and electromechanical losses in the measured electrical output. Therefore, the principal contribution of the present results is the consistent relative improvement obtained under identical experimental and electromechanical conditions rather than the absolute magnitude of Cp.

4.4 Practical Engineering Implications

The present results indicate that the aerodynamic shell can improve the low-speed operating behaviour of the aerofoil-assisted Savonius rotor by reducing the cut-in condition and increasing rotational speed, generated voltage, electrical power, Cp, and CT over the investigated range. These characteristics are potentially relevant to small distributed wind-energy systems, particularly where available wind conditions are close to the rotor cut-in threshold.

From an engineering perspective, the proposed shell is mechanically simple and can be integrated around the rotor without introducing an additional active aerodynamic control system. Its adjustable mounting also provides a practical means of modifying the rotor inflow direction during installation or experimental tuning. However, the present laboratory-scale prototype does not yet provide sufficient evidence to quantify annual energy production, economic payback, or lifecycle performance under real urban wind conditions.

The measured improvements were obtained under controlled wind-tunnel conditions with a fixed inflow direction. Actual urban wind environments are characterized by turbulence, rapid directional changes, shear, and intermittent gusts, which may alter the performance of both the rotor and shell. In addition, practical deployment would require consideration of structural support, shell alignment, environmental exposure, generator matching, bearing durability, maintenance accessibility, and protection against debris or accidental contact.

The present results therefore support the concept as a laboratory-scale performance-enhancement approach, but further field validation is required before commercial or urban energy-yield claims can be made. Future studies should combine long-term wind measurements with experimentally validated turbine power curves to estimate annual energy production and evaluate installation feasibility, maintenance requirements, and economic performance under representative operating conditions.

5. Conclusion

This study experimentally evaluated a Savonius vertical axis wind turbine incorporating NACA0024 aerofoil sections at the blade extremities together with an adjustable half-cylinder aerodynamic shell. The work was conducted as a proof-of-concept investigation to quantify the relative performance changes produced by the integrated configuration under controlled no-load and electrical-load conditions.

The shell-assisted configuration reduced the cut-in wind-tunnel speed from approximately 12 m/s to 9 m/s, corresponding to measured inlet velocities of about 10 m/s and 7 m/s, respectively. Rotor angular velocity increased by up to approximately 30% near the lower operating range, while no-load voltage improved by approximately 10–27%. Under electrical loading, peak power increased from approximately 0.05 to 0.12 W at 12 m/s, from 0.16 to 0.32 W at 15 m/s, and from 0.34 to 0.57 W at 18 m/s.

The power coefficient also increased consistently when the shell was installed. At 15 m/s, the maximum Cp increased from approximately 0.0086 to 0.0172, while comparable relative improvements were observed at 12 and 18 m/s. The torque coefficient exhibited a broader high-performance operating region, with peak CT increasing by approximately 68% at 15 m/s and 40% at 18 m/s. These results indicate that the shell-assisted rotor was able to maintain improved rotational and electrical performance over a wider range of electrical-loading conditions.

The principal contribution of the study lies in the experimental evaluation of the combined aerofoil-tip and adjustable-shell configuration rather than in either modification considered independently. The results demonstrate that the integrated arrangement can provide measurable relative improvements in cut-in behaviour, rotational speed, electrical output, Cp, and CT when compared with the same aerofoil-assisted rotor operating without the shell.

The absolute performance values should nevertheless be interpreted cautiously. The prototype operated at a low Reynolds number of approximately 1.4 × 10^4 to 2.8 × 10^4, had an aspect ratio of 2.0, and was tested without endplates. In addition, the rotor was positioned in the external jet downstream of the wind-tunnel outlet, where flow non-uniformity, turbulence, and geometric blockage effects may influence the measured coefficients. The measured electrical output also incorporates losses associated with the generator, rectifier, bearings, and shaft system. These factors contribute to the relatively low absolute Cp values obtained in the present study.

Additional limitations include the use of only two independent repetitions, evaluation of a single aerofoil profile and principal shell geometry, absence of direct flow-field or pressure measurements, limited wind-speed range, absence of yawed inflow conditions, and lack of long-term field and durability testing. The present results should therefore be considered laboratory-scale comparative evidence rather than direct predictions of full-scale urban turbine performance.

Future work should focus on systematic optimization of shell angle, rotor-shell gap, shell dimensions, aerofoil chord ratio, and aerofoil position, consistent with the strong sensitivity of VAWT performance to geometric parameters reported in previous studies (Ramlee *et al.*, 2022). Higher-Reynolds-number testing, incorporation of endplates, improved generator matching, and higher-aspect-ratio rotors should also be investigated (Kassab *et al.*, 2022). Direct aerodynamic characterization using CFD, PIV, or pressure measurements would help quantify the flow mechanisms responsible for the observed performance changes (Chaiyanupong & Chitsomboon, 2018). Finally, field testing under realistic turbulent and multidirectional urban wind conditions is required before the concept can be assessed for practical deployment and energy-yield applications.

Abbreviations

Abbreviation	Description
3D	Three-dimensional
AC	Alternating current
AR	Aspect ratio
BLDC	Brushless DC
CFD	Computational fluid dynamics
CR	Constant resistance
DOE	Design of experiments
HAWT	Horizontal-axis wind turbine
RPM	Revolutions per minute
SD	Standard deviation
SE	Standard error
SWT	Small wind turbine
SVAWT	Savonius vertical-axis wind turbine
TSR	Tip-speed ratio
VAWT	Vertical-axis wind turbine

Nomenclature

Symbol	Description
A	Rotor swept area (m^2)
A_r	Rotor projected area (m^2)
A_t	Wind-tunnel outlet area (m^2)
AR	Aspect ratio
c	Blade chord length (m)
C_p	Power coefficient
C_t	Torque coefficient
D	Rotor diameter (m)
H	Rotor height (m)
N	Rotor rotational speed (RPM)
P_e	Measured electrical output power (W)
r	Rotor radius (m)
R	Electrical load resistance (Ω)
Re	Reynolds number
V_e	Measured electrical voltage (V)
V_{in}	Inlet air velocity (m/s)
V_{out}	Outlet air velocity (m/s)
V_{ref}	Wind-tunnel reference speed (m/s)
V	Wind speed used in aerodynamic calculations (m/s)
β	Geometric rotor-to-outlet area ratio
η_v	Fractional outlet-velocity reduction
λ	Tip-speed ratio
μ	Dynamic viscosity of air (kg/(m·s))
ρ	Air density (kg/m^3)
σ	Rotor solidity
ω	Rotor angular velocity (rad/s)

Acknowledgements

The authors are grateful to all faculty and staff at Australian University (AU) for their support. Sincere thanks are extended to all members of the AU Workshop, especially Eng. Joji Abraham, for assistance in manufacturing the test bench, and to Eng. Bader Hadi Alazmi at the Fabrication Lab for producing the 3D-printed components.

Authors' Contributions

Mohamad Hussein Farhat: Funding acquisition, Investigation, Project administration, Supervision, Writing – review & editing. Ahmad Sedaghat: Conceptualization, Data curation, Formal analysis, Methodology, Project administration, Supervision, Writing – original draft. Nader Ghareeb: Investigation, Supervision, Validation. Mohamed El Badawy: Investigation, Supervision. Mohammad Nazififard: Writing – review & editing. Ali Mostafaeipour: Writing – review & editing.

Funding

This research was supported by the Australian University (AU)-Kuwait under grant number IRC-2024/2025-SRC-PR011.

Data Availability

Data from experiments are available upon reasonable request.

Declaration of Competing Interest

The authors declare no known financial or personal conflicts of interest.

Declaration of Generative AI Use

During the preparation of this work the authors used ChatGPT to improve language. After using this tool, the authors reviewed and edited the content as needed and take full responsibility for the content of the publication.

References

Abernethy, R. B., Benedict, R. P., & Dowdell, R. B. (1985). ASME Measurement Uncertainty. *Journal of Fluids Engineering, 107*(2), 161–164. https://doi.org/10.1115/1.3242450

Aboujaoude, H., Beaumont, F., Murer, S., Polidori, G., & Bogard, F. (2022). Aerodynamic performance enhancement of a Savonius wind turbine using an axisymmetric deflector. *Journal of Wind Engineering and Industrial Aerodynamics, 220*, 104882. https://doi.org/10.1016/j.jweia.2021.104882

Ahmad, M., & Rehman, I. (2023). Investigating Aerodynamic Performance of Vertical Axis Wind Turbines Using Computational Techniques. *Journal of Power Generation Technology, 1*(1), 20. https://doi.org/10.61369/JPGT.0568

Al-Gburi, K. A. H., Alnaimi, F. B. I., Al-quraishi, B. A. J., Tan, E. S., & Kareem, A. K. (2023). Enhancing Savonius Vertical Axis Wind Turbine Performance: A Comprehensive Approach with Numerical Analysis and Experimental Investigations. *Energies, 16*(10), 4204. https://doi.org/10.3390/en16104204

Altan, B. D., & Atılgan, M. (2008). An experimental and numerical study on the improvement of the performance of Savonius wind rotor. *Energy Conversion and Management, 49*(12), 3425–3432. https://doi.org/10.1016/j.enconman.2008.08.021

BIPM. (2023). Recent Progress in Design and Performance Analysis of Vertical-Axis Wind Turbines—A Comprehensive Review. https://www.mdpi.com/2227-9717/12/6/1094

Brusca, S., Lanzafame, R., & Messina, M. (2014). Design of a vertical-axis wind turbine: How the aspect ratio affects the turbine's performance. *International Journal of Energy and Environmental Engineering, 5*(4), 333–340. https://doi.org/10.1007/s40095-014-0129-x

Chaiyanupong, J., & Chitsomboon, T. (2018). Effects of turbulence models and grid densities on computational accuracy of flows over a vertical axis wind turbine. *International Journal of Renewable Energy Development, 7*(3), 213–222. https://doi.org/10.14710/ijred.7.3.213-222

Coleman, H. W. (with Internet Archive). (1999). *Experimentation and uncertainty analysis for engineers*. New York: Wiley. http://archive.org/details/experimentationu0000cole_2edi

Coleman, H. W., Steele, W. G., & Buzhuga, M. (2010). Experimentation, Validation, and Uncertainty Analysis for Engineers. *Noise Control Engineering Journal, 58*(3), 343. https://doi.org/10.3397/1.3383084

Deda Altan, B., & Gultekin, G. S. (2023). Investigation of Performance Enhancements of Savonius Wind Turbines through Additional Designs. *Processes, 11*(5), 1473. https://doi.org/10.3390/pr11051473

Didane, D. H., Behery, M. R., Al-Ghriybah, M., & Manshoor, B. (2024). Recent Progress in Design and Performance Analysis of Vertical-Axis Wind Turbines—A Comprehensive Review. *Processes, 12*(6), 1094. https://doi.org/10.3390/pr12061094

Farhat, M. H., Mehdizadeh, A., Sedaghat, A., Badawy, M. E., Djedi, B., Al-Khiami, M. I., Mostafaeipour, A., & Nazififard, M. (2025). Origami-inspired urban wind turbines: Scalable bladeless designs for decentralized renewable energy. *Green Technologies and Sustainability, 4*(1), 100253. https://doi.org/10.1016/j.grets.2025.100253

Ghareeb, N., Sedaghat, A., Farhat, M. H., Mehdizadeh, A., Ashtian Malayer, M., El Badawy, M., & Irannezhad, M. (2026). Experimental study on flexible and rigid 3D-printed Savonius vertical axis wind turbines with aerodynamic augmentation. *Wind Engineering*. https://doi.org/10.1177/0309524X261443931

Herath, M. T., Lee, A. K. L., & Gangadhara Prusty, B. (2015). Design of shape-adaptive wind turbine blades using Differential Stiffness Bend–Twist coupling. *Ocean Engineering, 95*, 157–165. https://doi.org/10.1016/j.oceaneng.2014.12.010

Hughes, I., & Hase, T. (2010). *Measurements and their Uncertainties: A practical guide to modern error analysis*.

Irawan, E. N., Shibuya, K., Yamashita, K., & Fujita, G. (2024). Unlocking the power of the wind: Innovations in smart hybrid vertical axis wind turbines. *International Journal of Renewable Energy Development, 13*(5), 974–981. https://doi.org/10.61435/ijred.2024.60354

Islam, M., Ting, D. S.-K., & Fartaj, A. (2008). Aerodynamic models for Darrieus-type straight-bladed vertical axis wind turbines. *Renewable and Sustainable Energy Reviews, 12*(4), 1087–1109. https://doi.org/10.1016/j.rser.2006.10.023

Kacprzak, K., Liskiewicz, G., & Sobczak, K. (2013). Numerical investigation of conventional and modified Savonius wind turbines. *Renewable Energy, 60*, 578–585. https://doi.org/10.1016/j.renene.2013.06.009

Kamoji, M. A., Kedare, S. B., & Prabhu, S. V. (2008). Experimental investigations on the effect of overlap ratio and blade edge conditions on the performance of conventional Savonius rotor. *Wind Engineering, 32*(2), 163–178. https://doi.org/10.1260/030952408784815826

Kamoji, M. A., Kedare, S. B., & Prabhu, S. V. (2009). Performance tests on helical Savonius rotors. *Renewable Energy, 34*(3), 521–529. https://doi.org/10.1016/j.renene.2008.06.002

Kassab, S. Z., Chemengich, S. J., & Lotfy, E. R. (2022). The effect of endplate addition on the performance of the Savonius wind turbine: A 3-D study. *Proceedings of the Institution of Mechanical Engineers, Part A: Journal of Power and Energy, 236*(8). https://doi.org/10.1177/09576509221098480

Kumar, K. S., Jaseel, M., Brintha, R., Devi, A., Jaiswal, K. K., Sangmesh, B. M., Suresh, A., & Balaji, P. S. (2024). Performance Enhancement of a Vertical Axis Wind Turbine (NACA 25112) Using Deflector Plates as an Augmenter. In P. Tambe, P. Huang, & S. Jhavar (Eds.), *Advances in Mechanical Engineering and Material Science* (pp. 227–233). Springer Nature Singapore. https://doi.org/10.1007/978-981-99-5613-5_18

Mohamed, M. H. (2012). Performance investigation of H-rotor Darrieus turbine with new airfoil shapes. *Energy, 47*(1), 522–530. https://doi.org/10.1016/j.energy.2012.08.044

Mohamed, M. H., Ali, A. M., & Hafiz, A. A. (2015). CFD analysis for H-rotor Darrieus turbine as a low speed wind energy converter. *Engineering Science and Technology, an International Journal, 18*(1), 1–13. https://doi.org/10.1016/j.jestch.2014.08.002

Mohamed, M. H., Janiga, G., Pap, E., & Thévenin, D. (2010). Optimization of Savonius turbines using an obstacle shielding the returning blade. *Renewable Energy, 35*(11), 2618–2626. https://doi.org/10.1016/j.renene.2010.04.007

Mrigua, K., Toumi, A., Zemamou, M., Ouhmmou, B., Lahlou, Y., & Aggour, M. (2020). CFD investigation of a new elliptical-bladed multistage Savonius rotors. International Journal of Renewable Energy Development, 9(3), 383–392. https://doi.org/10.14710/ijred.2020.30286

Mrigua, K., Zemamou, M., & Aggour, M. (2022). Numerical investigation of a new modified Savonius wind turbines. *International Journal of Renewable Energy Development, 11*(4), 1113–1123. https://doi.org/10.14710/ijred.2022.45799

Ramlee, M. F., Zishan, S., Muzammil, W. K., & Fazlizan, A. (2022). Numerical investigation of solidity effect based on variable diameter on power performance of H-type Darrieus vertical axis wind turbine (VAWT). *International Journal of Renewable Energy Development, 11*(3), 647–660. https://doi.org/10.14710/ijred.2022.44431

Rezaeiha, A., Kalkman, I., & Blocken, B. (2017). Effect of pitch angle on power performance and aerodynamics of a vertical axis wind turbine. *Applied Energy, 197*, 132–150. https://doi.org/10.1016/j.apenergy.2017.03.128

Roy, S., & Saha, U. K. (2015). Wind tunnel experiments of a newly developed two-bladed Savonius-style wind turbine. *Applied Energy, 137*, 117–125. https://doi.org/10.1016/j.apenergy.2014.10.022

Sedaghat, A., Djedi, B., Farhat, M. H., Al-khiami, M. I., & El Badawy, M. (2025). A novel origami inspired single rotor horizontal axis wind turbine. *Journal of Energy Systems, 9*(3), 271–291. https://doi.org/10.30521/jes.1723925

Sedaghat, A., Farhat, M. H., Djedi, B., Al-Khiami, M. I., & El Badawy, M. (2026). Experimental investigation of a wildlife-safe origami-inspired reaction-type wind turbine for sustainable urban energy systems. *International Journal of Renewable Energy Development, 15*(4), 708–718. https://doi.org/10.61435/ijred.2026.62526

Shahmari, M., Zarafshan, P., Kouravand, S., & Khashehchi, M. (2020). Design and Analysis of a Combined Savonius-Darrieus Wind Turbine for Irrigation Application. *Journal of Renewable Energy and Environment, 7*(3), 80–86. https://doi.org/10.30501/jree.2020.223382.1092

Shoukat, A. A., Noon, A. A., Anwar, M., Ahmed, H. W., Khan, T. I., Koten, H., Siddiqi, M. U. R., & Sharif, A. (2021). Blades optimization for maximum power output of vertical axis wind turbine. *International Journal of Renewable Energy Development, 10*(3), 585–595. https://doi.org/10.14710/ijred.2021.35530

Simão Ferreira, C., Van Kuik, G., Van Bussel, G., & Scarano, F. (2009). Visualization by PIV of dynamic stall on a vertical axis wind turbine. *Experiments in Fluids, 46*(1), 97–108. https://doi.org/10.1007/s00348-008-0543-z

Tummala, A., Velamati, R. K., Sinha, D. K., Indraja, V., & Krishna, V. H. (2016). A review on small scale wind turbines. *Renewable and Sustainable Energy Reviews, 56*, 1351–1371. https://doi.org/10.1016/j.rser.2015.12.027

Ushiyama, I., & Nagai, H. (1988). Optimum Design Configurations and Performance of Savonius Rotors. *Wind Engineering, 12*(1), 59–75.

Wong, K. H., Chong, W. T., Sukiman, N. L., Poh, S. C., Shiah, Y.-C., & Wang, C.-T. (2017). Performance enhancements on vertical axis wind turbines using flow augmentation systems: A review. *Renewable and Sustainable Energy Reviews, 73*, 904–921. https://doi.org/10.1016/j.rser.2017.01.160

Wang, X.-H., Foo, J. S.-Y., Fazlizan, A., Chong, W.-T., & Wong, K.-H. (2024). Effects of endplate designs on the performance of Savonius vertical axis wind turbine. *Energy, 310*, 133205. https://doi.org/10.1016/j.energy.2024.133205

Youssef, K. M., El Kholy, A. M., Hamed, A. M., Mahmoud, N. A., El Baz, A. M., & Mohamed, T. A. (2020). An innovative augmentation technique of Savonius wind turbine performance. Wind Engineering, 44(1). https://doi.org/10.1177/0309524X19849860